The Cryosphere

Supplement of

Four decades of Antarctic surface elevation changes from multi-mission satellite altimetry

Ludwig Schröder et al.

Correspondence to: Ludwig Schröder (ludwig.schroeder@tu-dresden.de)

S1 Data

Table S1: Temporal coverage of the different missions altimetry data.

Mission	From	To
Seasat	1978-07-06	1978-10-10
Geosat	1985-04-01	1989-09-26
ERS-1	1991-08-03*	1996-06-02
ERS-2	1995-05-14	2003-07-02
Envisat	2002-05-14	2012-04-08
ICESat	2003-02-20	2009-10-11
CryoSat-2	2010-07-16	2017-12-31

* ERS-1 data before 1992-04-14 has not been used, see A.2.

S1.1 Seasat/Geosat

The observation data of Seasat and Geosat were obtained from the Radar Ice Altimetry project at Goddard Space Flight Center (GSFC, `https://icesat4.gsfc.nasa.gov/index.php`). We used the Ice Data Record (IDR) and for waveform retracking the corresponding Waveform Data Record (WDR). Orbit corrections for JGM-3 orbits were applied and measurements excluded if the noise level of the waveform was too high (flagged in WDR).

In order to make the GSFC data comparable to our reprocessed data in the crossover analysis (Sect. 2.3) we furthermore used the flags indicating that the GSFC-retracking was not successful (leading edge definition failed or problems occurred during retracking). These retracking flags, however, do not apply to our reprocessed data, used in all following processing.

S1.2 ERS-1/2

For ERS-1 and ERS-2 the SGRD data from the ESA REAPER (Reprocessing altimeter products for ERS) project (Brockley et al., 2017) was used. We excluded measurements where the flags in the data indicated a poor orbital or range measurement quality, where the tracking was lost, where waveforms are corrupted (e.g. due to high noise) and where time jumps in the data occurred as reported by the pre-release calibration/validation ("RA L2 Validation Report", `https://earth.esa.int/documents/10174/1511090/REA-TR-VAL-L2-7001-3-1.pdf`).

Our accuracy and precision tests using crossover (see Sect. 2.2) showed, that the early mission phases of ERS-1, prior to 1992-04-14, contain many outliers which could not be identified by any flag or suspicious value. Thus, we decided to exclude all data of this period from our analysis.

S1.3 Envisat

For Envisat we used the SGDR V2.1 data from ESA. Here we used the Ku-band measurements of its altimeter system RA-2 acquired during the entire operational period. To remove potentially corrupted observations from the data, we used the *measurement confidence flags* to find recorded distances out of range and to identify problems in the onboard processing and data handling, in the ultra stable oscillator, the automatic gain control or in the waveform samples. We furthermore used the *fault identifier*, the *tracker range validity flag* and the *ICE1 retracking validity flag* to exclude invalid measurements.

S1.4 ICESat

For ICESat the Release 634 GLA12 dataset from the National Snow and Ice Data Center (NSIDC) was used. We excluded all data where flags indicate a degraded orbit accuracy (e.g. due to off-nadir

operation or orbit maneuvers). We also removed data where the attitude flag indicates any problem with star trackers, gyro or the laser reference sensor. In order to exclude data affected by forward scattering in clouds or drifting snow (e.g. Siegfried et al., 2011), we reject all returns with a gain value exceeding 200, with a reflectivity below 10%, with a misfit between the received waveform and the Gaussian model exceeding 0.03 V or where more than one waveform was detected (Bamber et al., 2009). As the elevation measurements of all other missions refer to the WGS84 ellipsoid, we applied the WGS84 ellipsoid corrections. Furthermore, we applied the saturation correction (Fricker et al., 2005) and corrected the inter-campaign biases according to Schröder et al. (2017).

S1.5   CryoSat-2

We used the CryoSat-2 L2I product from ESA in the recent processing version Baseline C. For LRM we excluded all data where the *height error flag* indicates problems in the overall height determination. For SARIn mode, we used the retracking scheme described in Helm et al. (2014) using a 40%-TFMRA retracker. The Star Tracker mispointing angles, corrected for the aberration of light, were applied prior the phase processing. This correction is explained in Scagliola et al. (2017) and the data set provided by ESA. "Bad waveforms" are screened using a waveform filter (Helm et al., 2014).

S2   Reprocessing of radar altimetry

To form a consistent data base, the conventional pulse limited radar altimeter (PLRA) data from the different missions has been reprocessed using a common retracking technique and relocation method. We use the OCOG retracker (Wingham et al., 1986) and the refined relocation method by Roemer et al. (2007) as described in Sect. 2.2. To exclude data from corrupted waveforms in our reprocessed data, we calculated a signal-to-noise ratio (SNR) between the OCOG amplitude and the noise level. We excluded all shots where the SNR is smaller than 3.

In order to assess the precision of the data we calculate near time ($\Delta t < 31d$) ascending-descending crossover differences. As a reference we use the widely applied data processing version of each data center with functional fit retracker (GSFC Version 4 β-retracker for Seasat and Geosat, the ICE-2 retracker for ERS and Envisat and the default CFI retracker for CryoSat-2) and the respective slope correction (direct slope correction for GSFC, relocated by mean surface slope for ESA). We compare these standard products with our reprocessed data at 3 different retracking thresholds levels (10%, 20% and 50%). Figure S1 contains the results, binned against surface slope (as in Fig. 2).
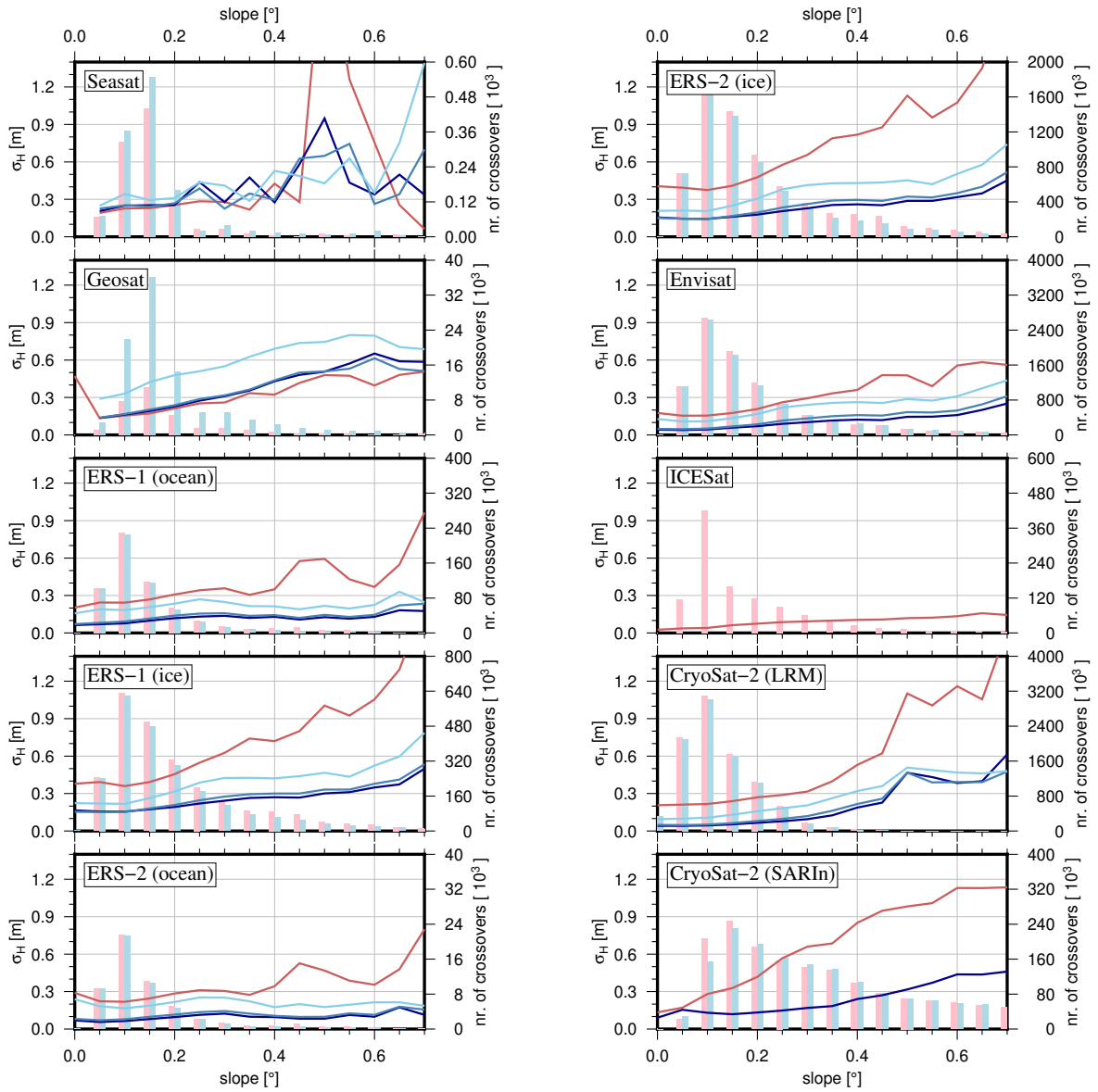
Figure S1: Precision of different processing versions of altimeter measurements from near time (<31 days) crossovers, binned against slope. Red curve: functional fit data provided by the respective data centers (see description above). Light, medium and dark blue curves: Data reprocessed in this study with 50%-, 20%- and 10%-threshold retracker, respectively, relocated using the refined method. For CryoSat-2 SARIn, dark blue stands for 40%-TFMRA retracked data (Helm et al., 2014). Vertical bars: number of crossovers for the standard product (red) and our 10% threshold retracked data (blue).
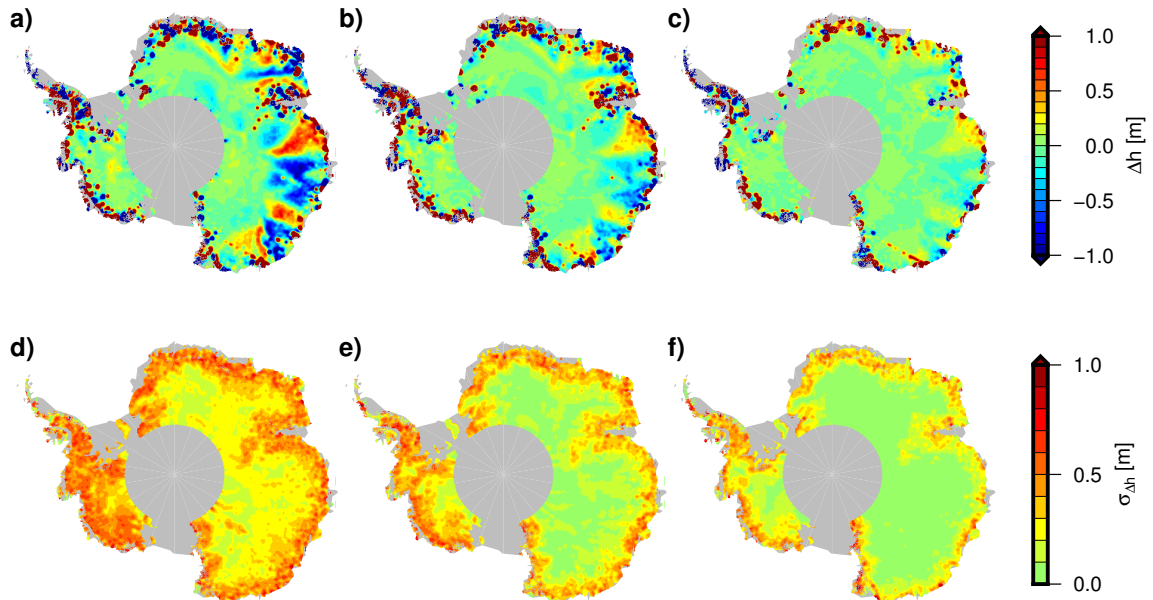
Figure S2: Median offset (**a-c**) and MAD (**d-f**) over $10\,\mathrm{x}10\,\mathrm{km}$ from short term ($\Delta t < 31d$) crossover differences between ascending and descending orbits for 3 different processing versions of the Envisat data: **a/d)** ESA version with ICE-2 retracker, **b/e)** ESA version with ICE-1 retracker and **c/f)** our reprocessed data with 10%-threshold retracker.

A spatial pattern of the ascending-descending crossover differences (A-D bias) has been noted by Legrésy et al. (1999) and Arthern et al. (2001). However, as shown by Helm et al. (2014), this bias is strongly dependent on the choice of the retracker. Comparing the near time A-D crossover differences of the ESA product of Envisat using the ICE-2 retracker, the ICE-1 retracker (threshold level 30%) and our reprocessed 10% threshold OCOG retracker (Fig. S2) shows that the A-D bias has been significantly reduced. While the ICE-2 data show a well pronounced pattern in the coastal regions with magnitudes of up to a meter, the biases in our product are significantly smaller. In coastal Princess Elizabeth Land (70-90°E), the maximum magnitude still reach $30\,\mathrm{cm}$, while elsewhere, the biases do not exceed $15\,\mathrm{cm}$. The corresponding median absolute deviations (MAD) in the map below show, that these biases are below the remaining noise level.

S3 Processing of multi-mission SEC time series

S3.1 Single-mission time series

The single-mission time series are regained from the parameters and monthly averages of the residuals as described in Sect. 3.2. These residuals contain the noise of the measurements and modeling errors (as e.g. nonlinear surface elevation changes or a more complex topography). The monthly average $\overline{res}$ represents the time-dependent modeling errors, i.e. the seasonal and interannual signal, while the remaining modeling errors (i.e., of the topography fit and the backscatter correction) and the noise is subsumed under the standard deviation $\sigma_{\overline{res}}$ of the monthly average. Therefore, we use $\sigma_{\overline{res}}$ as uncertainty estimate for our time series. If this value is larger than $10\,\mathrm{m}$ or if it cannot be computed as only one observation is available for this month, we exclude this epoch from the time series.

Figure S3 shows the median of the monthly uncertainty estimates for each data set (before additional uncertainties are added due to corrections in the following steps). In the coastal regions, the observations of Seasat are very sparse, while Geosat data has a high uncertainty. Nevertheless, on the plateau, the noise of the Seasat and Geosat observations is only slightly higher than for the ice mode of ERS. Here, the advantages of both observation modes of ERS become evident. The

ocean mode provides less noise on the plateau while the ice mode data have a much better coverage in the margins. The high noise of CryoSat-2 SARIn near the coast can be explained by its high resolution. This demonstrates that a planar surface of 2 km (which is a compromise between the conditions provided by the different missions and modes involved) cannot adequately represent the detailed topography, sampled by the SARIn data there.
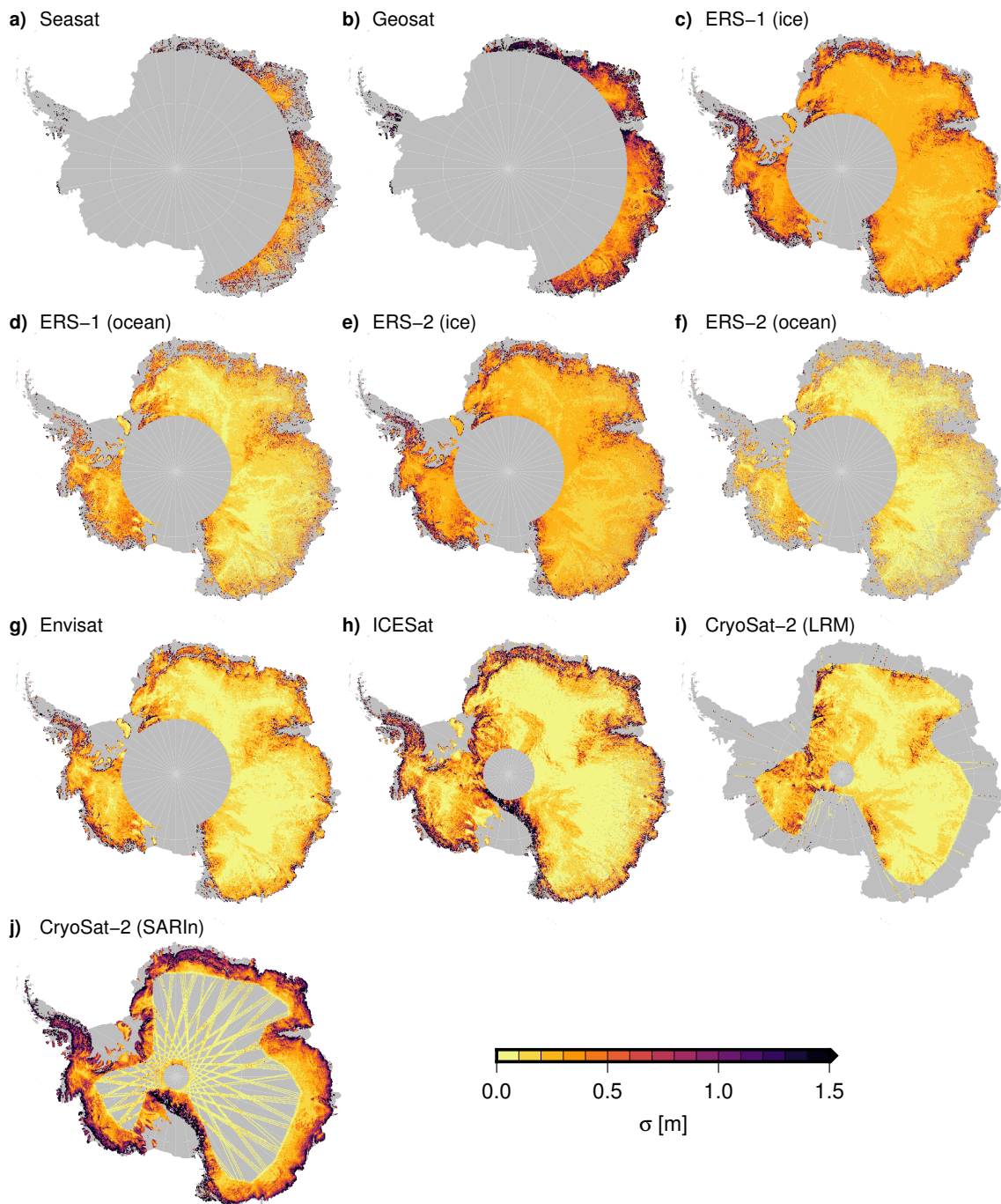

Figure S3: Uncertainty estimates of single-mission time series (median over all epochs of each cell).

S3.2 Merging PLRA time series

As described in Sect. 3.3, the PLRA satellites sample the topography in the same way and, hence, offsets to merge the time series are valid over larger regional scales. If two missions overlap in time, we use the overlapping epochs to obtain the spatial pattern of the calibration offset. Otherwise, offsets can only be determined where we can assume that the surface elevation change is stable over time. As this cannot deliver the full spatial pattern of offsets, we use a robust overall average to calibrate these missions.

After the offsets are determined as described in the following two subsections, the PLRA time series are corrected and combined. The respective uncertainty estimates are added to the time series and if the data sets overlap, they are averaged using weights according to their uncertainties.

S3.2.1 Offsets from overlapping epochs

For the missions ERS-1, ERS-2, Envisat and CryoSat-2 in low resolution mode (LRM) we use overlapping epochs for calibration. Therefor, we calculate the time series differences at each cell and for each month observed simultaneously and use the temporal median over all overlapping epochs. In order to obtain an uncertainty estimate for these offsets, we use the MAD of the differences at these epochs. As, however, some outliers might exist in these grids, we apply a spatial outlier filter. We calculate a moving spatial median over 100x100 km and remove any offset that deviates more than 30 cm from the filtered grid. We also exclude any value where the spatial median has been calculated from less than 20 values, i.e. where not enough control data existed. To smooth the offsets and fill the gaps between the ground tracks of the overlapping period, we applied a gaussian filter with $\sigma = 20$ km. This smoothing was also applied to the squared uncertainties in order to get gridded offset uncertainties.

To form a homogeneous time series, all missions have to be corrected towards one selected reference mission. We chose Envisat for this purpose. In the case of ERS-1, which has no overlap with this reference mission, the offsets need to be summed up. Due to the better spatial and temporal coverage of ERS's ice mode, the ocean mode biases have been determined w.r.t. ice mode and added to the specific ice mode offset. For ERS-1 in ocean mode ($ERS1_O$), this is calculated as

$$\Delta h_{ERS1_O - ENVI} = \Delta h_{ERS1_O - ERS1_I} + \Delta h_{ERS1_I - ERS2_I} + \Delta h_{ERS2_I - ENVI} \tag{S1}$$

The squared uncertainties of the individual offsets were added up. Figure S4 shows the offsets, respectively the sums of offsets, which have been applied to the PLRA single-mission time series.

a) ERS–1 (ice)

b) ERS–1 (ocean)

c) ERS–2 (ice)

d) ERS–2 (ocean)

e) CryoSat–2 (LRM)

−2.0 −1.5 −1.0 −0.5 0.0 0.5

$\Delta h_{Envisat}$ [m]

0.0 0.5
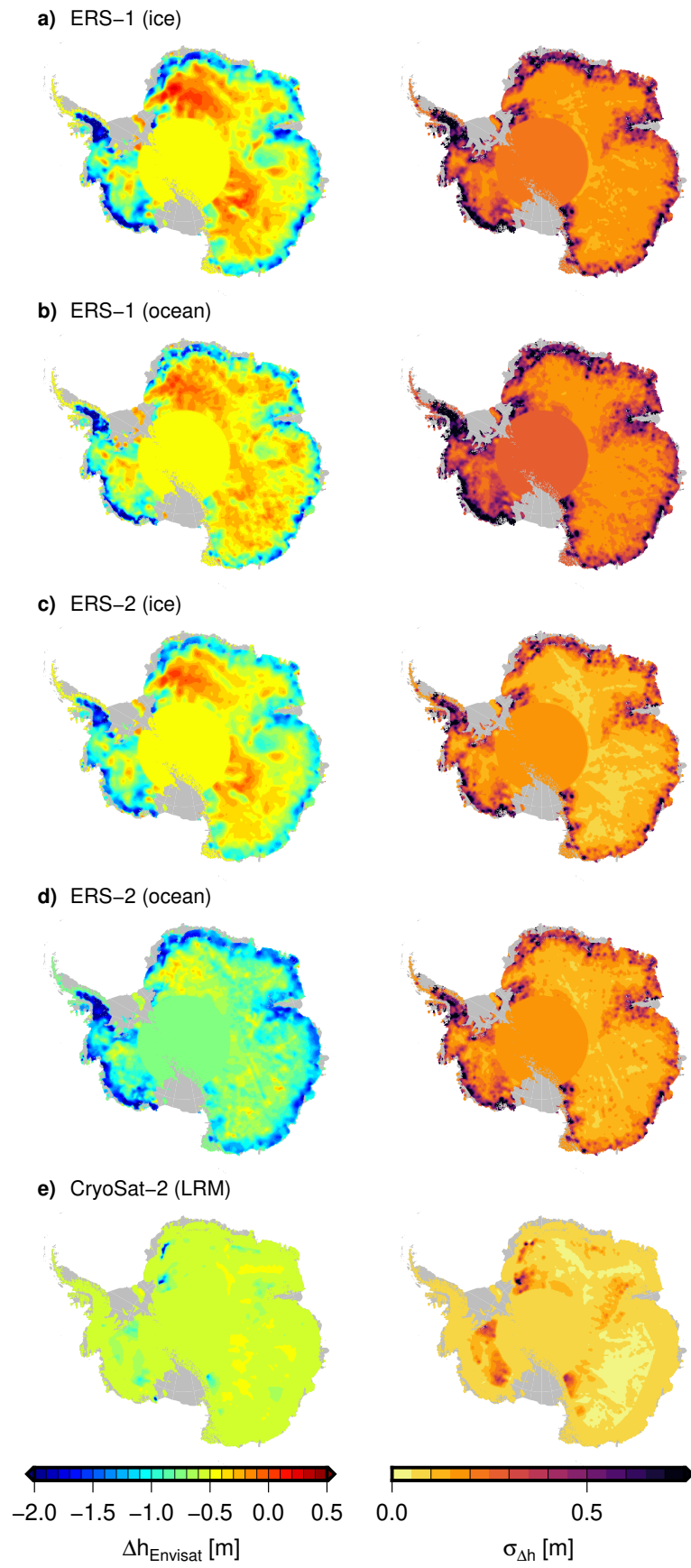
$\sigma_{\Delta h}$ [m]

Figure S4: Offsets applied for calibrating the PLRA data with our reference mission Envisat and their uncertainty estimates.
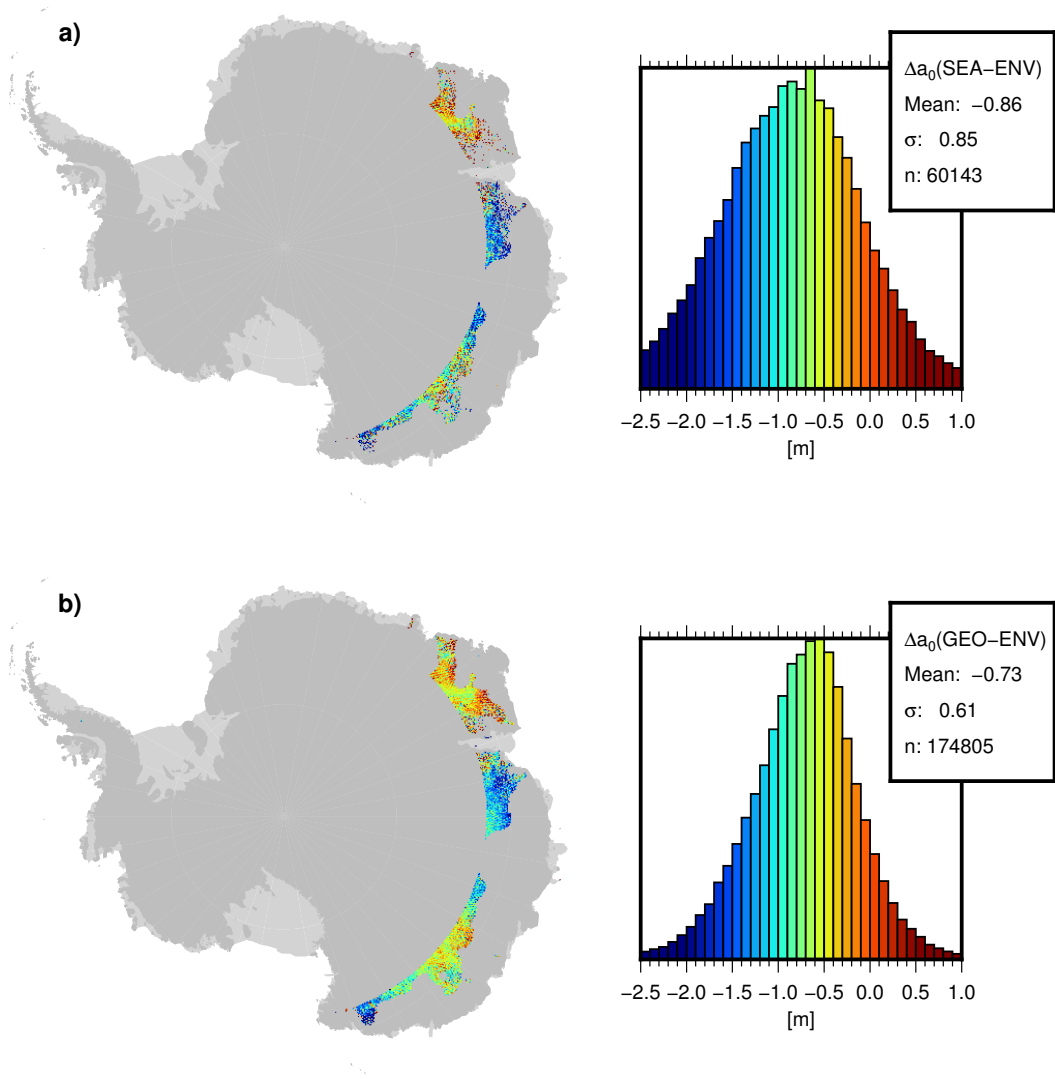
7

S3.2.2   Offsets from stable linear trend

Figure S5: Offsets between **a** Seasat and Envisat and **b** Geosat and Envisat from cells which satisfy our criteria of a stable linear SEC rate.

As described in Sect. 3.3.1, the calibration offsets for Seasat and Geosat are determined from the regions of the AIS, where the a posteriori standard deviation of the trend fit and the FDM indicate a stable linear trend. Figure S5 shows where $\sigma_{dh/dt} < 1\,\mathrm{cm/yr}$ and $RMS_{FDM} < 20\,\mathrm{cm}$ are true. The offsets between the respective missions and Envisat reveal that there is a spatial pattern, similar as for later missions. However, these offsets do not represent the whole spatial pattern. Especially in the coastal regions, interannual variations in the elevation changes do not allow the calibration. As it can be seen from the overlapping missions (Fig. S4), a simple extrapolation would not be adequate. Furthermore, our criteria serve as an upper boundary for the variations. Smaller interannual variations may still be present and cannot be separated from the true pattern of offsets. Hence, for the sake of robustness, we decided to apply a mean offset. Here, the influence of remaining interannual variations mitigates significantly over a continental scale. To account for the larger uncertainties, we use the standard deviation of all offsets (0.85 m for Seasat, 0.61 m for Geosat) as the uncertainty of the calibration, which is significantly larger than for the overlapping missions (see uncertainty maps in Fig. S4).

To check the plausibility, we compare these offsets to the values used in other studies. Davis

et al. (1998) report an inter-mission bias of 27±4 cm between Seasat and Geosat from crossover differences over the global oceans. In the notes, they further discuss that other investigations obtained lower sea-surface based biases (e.g. 22±4 cm by G. Kruizinga [thesis, University of Texas, Austin (1997)]). Fricker and Padman (2012) use Seasat in combination with ERS1, ERS-2 and Envisat. They combine these biases of Davis et al. (1998) with other biases for Envisat and finally apply an offset of -0.77 m between Seasat and Envisat.

Within the standard deviation of our estimates, these differences (in the order of magnitude of about a decimeter) are small, but not negligible. However, over ice sheets, the anisotropic surface can have a strong influence on these biases. Legrésy et al. (1999) analyze the A-D biases of ERS-1 and find a clear relationship between the linear polarized measurements and the surface shape. They conclude that merging the circularly polarized altimeter measurements of Seasat and Geosat with linearly polarized measurements of ERS (as well as Envisat) over ice sheets requires extreme care. Thus, we do not rely on the sea-surface based calibration and use the biases determined here.

S3.3 Merging different techniques

As described in Sect. 3.3.2, offsets of different observation techniques have to be determined for each cell individually due to the different topography sampling. Therefore, we determine an elevation for the reference epoch 09/2010 for each technique and reduce each time series by that reference elevation. To account for uncertainties of the reference elevations, the standard deviations of these fits are combined with the other uncertainty components of the time series by adding the standard uncertainties in square.

Before the final merging step, we remove remaining outliers in the technique specific time series. Especially for the early missions, gross orbit errors offset whole satellite passes. Such systematic outliers cannot be identified by the standard deviation of the residuals. Only after calculating the SEC by removing the reference elevation, they show up clearly against their neighboring passes. Therefore, we utilize a floating median as a robust low-pass filter to identify such outliers. Over a window of 40 km in space and 12 months in time, we calculate the floating median and median absolute deviation (MAD). The MAD indicates the variations on a regional scale and the shorter time scale (i.e. mainly the seasonal signal). To identify probable outliers, we use two thresholds. If the MAD exceeds 50 m, the window is very likely dominated by very noisy data. If, furthermore, the absolute difference $|SEC_j - \mathrm{Median}(SEC_{window})|$ exceeds $0.5\,\mathrm{m} + 3 \cdot MAD_{window}$, the data differs significantly from the usual variation in this region and is excluded as well. Near outlet glaciers, where the gradient is large, the $3 \cdot MAD$ will remove unusual outliers, while in regions with very low variation, the MAD might become very small. Therefore, we add 0.5 m to the outlier criterion to allow for some variation in the data.

The final combination of the techniques is performed using a weighted spatio-temporal averaging with 10 km σ gaussian weights in spatial domain and including the two consecutive epochs in the temporal domain to reduce the noise of a single pass. All filtered time series data within a 3σ (30 km) distance in this 3 month window are included but a value is only calculated if at least one data point is closer than 20 km and the central month contains data as well. Hence, the merged multi-mission SEC_m is calculated from all SEC_j (for PLRA, SARIn data and laser altimetry) within the given spatio-temporal radius as

$$SEC_m = \frac{\sum W_j \cdot SEC_j}{\sum W_j}. \tag{S2}$$

The weights for each contributing SEC j are specified according to the respective uncertainty estimate σ_j and the distance to the interpolated location $d_{j,m}$ as

$$W_j = e^{-\frac{d_{j,m}^2}{(10\,\mathrm{km})^2}} / \sigma_j^2. \tag{S3}$$

We calculate the uncertainty estimate as

$$\sigma_m^2 = \frac{\sum W_j \cdot \epsilon_j^2}{\sum W_j} + \min(\sigma_j)^2. \tag{S4}$$

The first term on the right hand side of this equation is the standard deviation of the contributing SEC_j from the error propagation, using the residuals of the observations $\epsilon_j = SEC_j - SEC_m$ and the respective weights. This, however, assumes uncorrelated errors. A systematic error, which influences all measurements within this region, would not be included. Besides the observational noise, our a priori σ_j for each observation include also the systematic errors of the calibration and of the determination of the reference elevation. As a conservative estimate for the systematic effects, we chose the smallest a priori uncertainty in the respective radius and add this value to the standard deviation of the smoothed value.

According to the spatial smoothing implied by our Gaussian weighting function, we reduce our spatial grid resolution to $10 \times 10\,\mathrm{km}$. We did not interpolate a value to cells which are mainly covered by rocks (Burton-Johnson et al., 2016) or outside of the grounded ice sheet (according to the definition of drainage basins).

In the spatial domain, the criterion of a maximum distance of $20\,\mathrm{km}$ to any observational data guarantees that a value is only calculated for a $10 \times 10\,\mathrm{km}$ cell if we have any data within the radius of a pulse-limited footprint. Grid cells with no valid data within this distance will be left empty and treated as *unobserved*. Similarly, in the temporal domain we calculate grids only if the central month of our 3-month moving average really contains observational data.
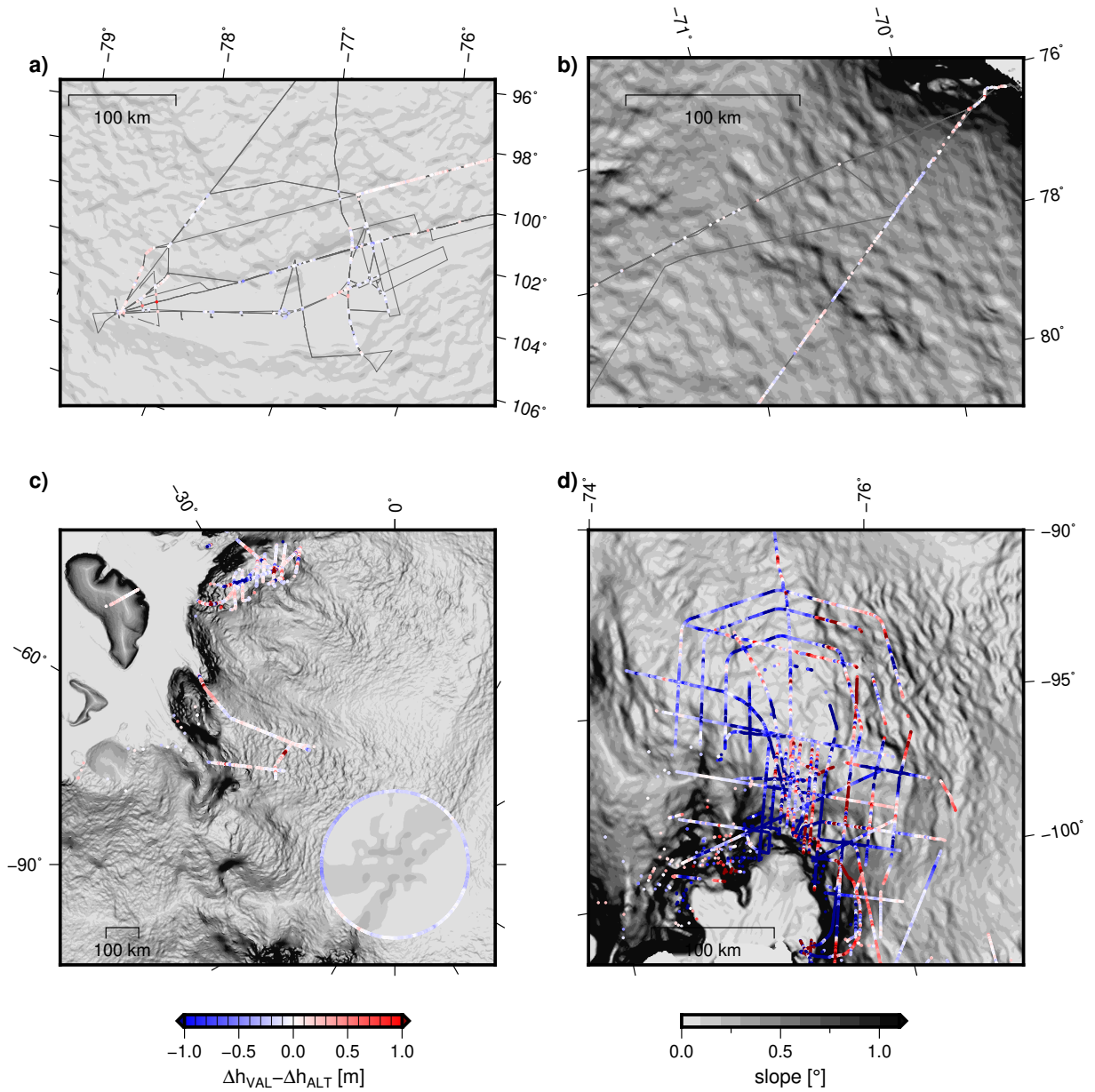
S4 Comparison of SEC with independent data

Figure S6: Detailed maps of Fig.7 a and d of the differences in observed elevation changes between altimetry and validation data for some key regions: Kinematic GNSS - Altimetry at **a)** Lake Vostok and **b)** near Progress Station; Operation IceBridge - Altimetry at **c)** the South Pole and Queen Elizabeth Land and **d)** at Pine Island Glacier.
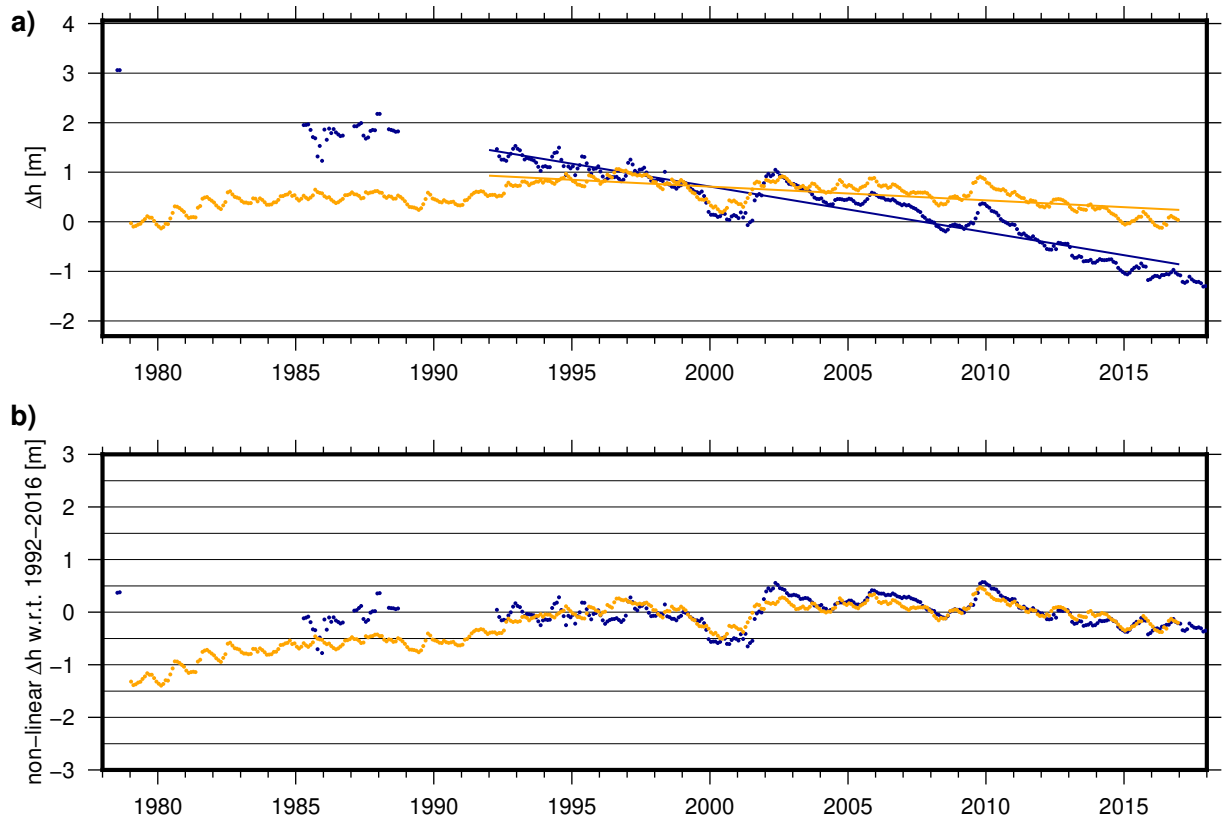
Figure S7: Example for the cross-validation of the altimetry time series (blue) and the FDM (orange). **a)** Total elevation change of both time series for point B at Totten Glacier (cf. Fig. 10b and Tab.2). The solid lines represent the linear trend for 1992-2016 fitted to each time series. **b)** Time series of nonlinear signal component after removing the linear trend from the altimetric SEC and the FDM.
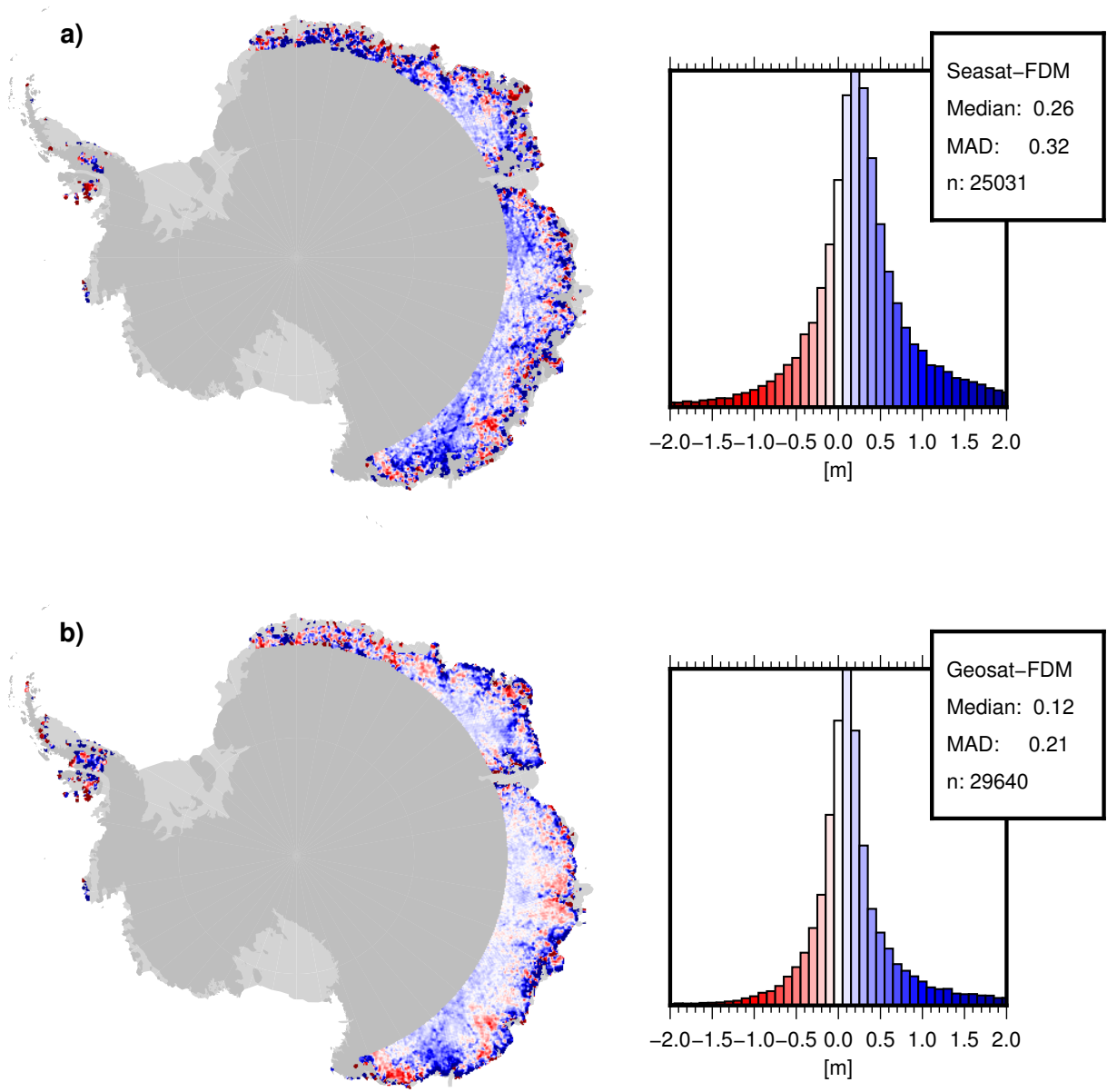
Figure S8: Anomaly differences between **a** Seasat and the FDM and **b** Geosat and the FDM after removing a linear trend, fitted over 1992-2016, from each cell.
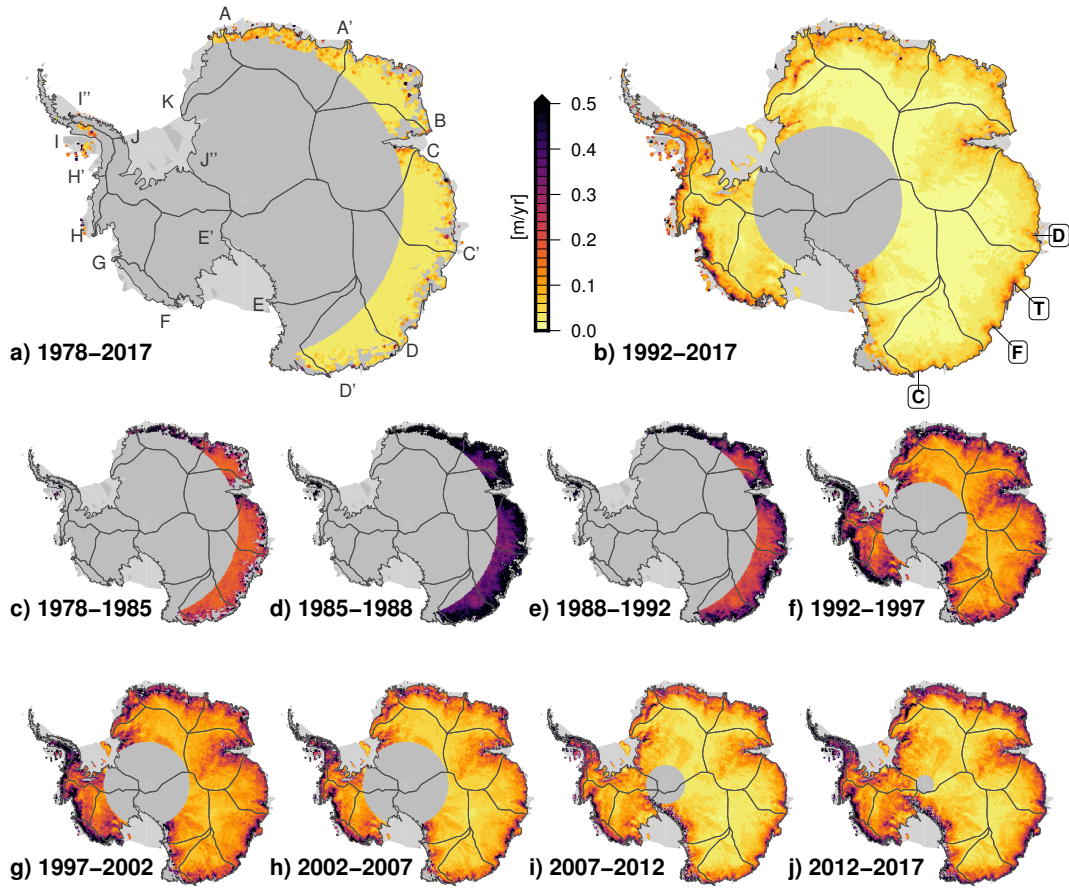
S5 Surface elevation change

Figure S9: Standard deviation of the multi-mission surface elevation change rates in Fig. 9.

Table S2: Coordinates (polar stereographic, EPSG:3031) and selected results for the points in Fig. 10 (regions: **a** Pine Island Glacier, **b** Totten Glacier, **c** Shirase Glacier and **d** Lake Vostok). The data represent the mean value of the SEC w.r.t 09/2010 over one year. The corresponding uncertainty is the RMS of all uncertainty estimates within this year.

Region	Point	x [m]	y [m]	$\overline{SEC}_{1978}$	$\overline{SEC}_{1988}$	$\overline{SEC}_{1998}$	$\overline{SEC}_{2008}$	$\overline{SEC}_{2017}$
a	A	-1590000	-110000	-	-	9.30±1.21	2.68±0.40	-8.91±0.94
a	B	-1590000	-160000	-	-	13.70±1.71	3.81±0.55	-8.95±1.25
a	C	-1580000	-200000	-	-	20.66±2.10	5.97±0.74	-10.96±2.22
a	D	-1580000	-240000	-	-	30.41±7.57	7.91±1.88	-10.82±2.74
b	A	2080000	-790000	-0.61±1.07	-0.57±0.75	-0.29±0.74	-0.08±0.18	-0.38±0.52
b	B	2160000	-890000	2.91±1.26	1.86±1.15	0.83±0.69	-0.09±0.25	-1.21±0.66
b	C	2220000	-960000	12.18±3.83	8.28±1.34	3.32±1.48	0.33±0.42	-2.83±1.05
b	D	2260000	-1000000	-	14.87±3.88	8.09±4.54	1.92±1.46	-7.60±4.43
c	A	1380000	1450000	-0.02±1.04	-0.11±0.82	-0.22±0.50	-0.30±0.21	0.18±0.26
c	B	1380000	1530000	0.16±1.11	-0.23±0.90	-0.61±0.62	-0.55±0.26	0.23±0.90
c	C	1380000	1600000	0.77±1.34	0.07±1.54	-0.75±1.18	-0.64±0.39	0.11±0.98
c	D	1380000	1660000	0.53±1.08	-0.20±2.75	-2.29±1.77	-0.45±0.66	1.61±1.52
d	A	1250000	-360000	-	-	-0.05±0.24	-0.02±0.06	0.02±0.08
d	B	1310000	-370000	-	-	-0.05±0.25	-0.03±0.06	0.05±0.08
d	C	1380000	-370000	-	-	0.02±0.26	-0.02±0.07	0.04±0.10
d	D	1420000	-340000	-	-	0.07±0.22	-0.02±0.07	0.03±0.09

14

S6   Ice sheet mass time series
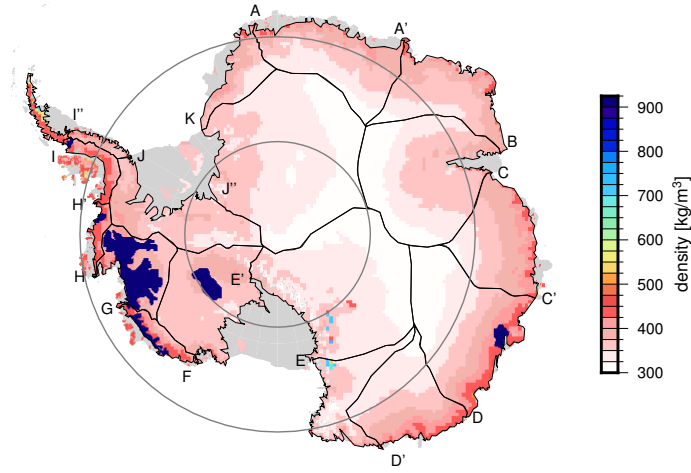
S6.1   Basins and density

Figure S10: Density mask, adapted after McMillan et al. (2014), with varying firn density from Ligtenberg et al. (2011). The black lines mark the borders of the drainage basins, the gray circles the latitude 72°S and 81.5°S which are the southern limit of several altimetry missions, used.

Table S3: Area [10^3 km^2] of each basin within the respective zones covered by different missions.

Region	Overall	<81.5°S	<72°S
ANT	11892	9391	2913
APIS	232	232	134
EAIS	9620	7764	2779
WAIS	2038	1394	0
A-A'	770	770	233
A'-B	651	651	510
B-C	1310	1310	173
C-C'	707	707	608
C'-D	1161	1161	691
D-D'	696	696	453
D'-E	427	427	93
E-E'	1580	813	0
E'-F	803	450	0
F-G	131	131	0
G-H	419	419	0
H-H'	65	65	0
H'-I	110	110	41
I-I''	61	61	61
I''-J	61	61	31
J-J''	619	327	0
J''-K	2055	966	0
K-A	259	259	15

S6.2 Uncertainty estimates

In the conversion of the monthly SEC grids into mass anomaly grids, the corrections for GIA dh_{GIA}, the factor for elastic bedrock response α and the density mask values ρ are applied as described in Sect. 5.2. A correction for firn compaction, which would lead to an elevation change without a change in mass, has not been applied here. This effect affects mainly short time scales. Over long time scales, which is the main scope of this paper, only a persistent instability in atmospheric conditions would cause an effect of firn compaction. Such an instability, however, wouldn't be detectable even by firn modeling due to the steady state condition.

The uncertainty estimate for the resulting mass grids are obtained by propagating the formal uncertainties of the contributing data. Here, we denote the uncertainty estimate of the merged SEC grids, obtained from Eq. (S4), by σ_{SEC}. As an estimate for the uncertainty of the density ρ, we use $\sigma_\rho = 100\,\mathrm{kg/m^3}$ as in Groh et al. (2014), which accounts for uncertainties due to firn compaction as well. For the GIA correction, we obtain an uncertainty estimate σ_{GIA} from the difference between the models of Ivins et al. (2013) and Whitehouse et al. (2012), propagated to the respective epoch. The uncertainty of the elastic bedrock response factor α is considered negligible, compared to σ_{SEC}, as it is directly related to the SEC itself. Hence, the gridded values of mass change dM per area element and the related formal uncertainties σ_{dM} are calculated as

$$
\begin{aligned}
dM &= \rho \cdot \alpha (dh_{SEC} - dh_{GIA}) \\
\sigma_{dM}^2 &= \rho^2 \cdot \alpha^2 (\sigma_{SEC}^2 + \sigma_{GIA}^2) + \alpha^2 (dh_{SEC} - dh_{GIA})^2 \cdot \sigma_\rho^2
\end{aligned}
\tag{S5}
$$

When summing up the mass changes over a basin, however, not all of these uncertainties can be considered uncorrelated. Uncorrelated uncertainties would average out when summed up over many grid cells. However, correlated uncertainties influence all cells in a certain distance in a systematic manner (as e.g. uncertainties in the density over larger regions) and, hence, can lead to much larger uncertainties of the sums. Similar to Wingham et al. (1998), we calculated the autocovariance of the SEC in different regions and found sufficient decorrelation for distances longer than $50\,\mathrm{km}$. This radius corresponds to an area of $\pi \cdot (50km)^2$ or 78.5 grid-cells of $A{=}10\,x10\,\mathrm{km}$. Therefore, we applied a scaling factor of $\beta = 78.5$ to the squared uncertainties in order to account for the autocorrelation over the area.

Besides the uncertainty of the observed cells o, an additional uncertainty in the sums comes from the unobserved cells u. To account for the changes which could not be observed by altimetry, we used the mass trends from GRACE. They originate from spherical harmonics and, hence, are free of gaps. We calculated a dM grid for the respective epoch from the linear GRACE trends and summed those dM up over all cells which are not observed by altimetry within a basin. Summed up over all observed (o) and unobserved (u) cells of the respective basin, these two components are used to obtain the total uncertainty σ_Σ for each epoch as

$$
\sigma_\Sigma^2 = \sum_o A \cdot \beta \cdot \sigma_{dM,o}^2 + \sum_u A \cdot dM_u^2,
\tag{S6}
$$

These uncertainty estimates are displayed in the plots of summed mass time series (Figs. 11, 12 and 13).

S6.3 Correlation with independent data

A comparison of the mass change rates obtained from altimetry and GRACE in Tab. S4 shows that GRACE observes a significantly larger mass gain of the EAIS (see also Fig. 11). Also for the APIS, there are substantial differences. The correlation coefficients r have been calculated from the anomalies of both time series. For the total Antarctic time series ($<81.5°$S), the correlation coefficient between altimetry and GRACE (for the time period 2002-2016) of 0.96 demonstrates that the interannual variability, measured by both types of observations, agrees very well. At the EAIS, the signals are more dominated by remaining issues in the processing of both data sets.

Table S4: Comparison of the mass time series for the AIS ($<81.5°$S) between the altimetry and the two independent datasets over simultaneously observed periods. The mass change rates for the corresponding data and time interval are calculated as in Tab. 2. The correlation coefficients r refer to the respectively detrended anomalies.

| | 2002-2016 | | | 1992-2016 | | |
| | dM/dt [Gt/yr] | | | dM/dt [Gt/yr] | | |
region	altimetry	GRACE	r_{GRACE}	altimetry	SMBA	r_{SMBA}
AIS	-109.9±15.6	-88.7	0.962	-84.7±15.5	-2.2	0.604
EAIS	9.6±6.9	42.1	0.558	4.9±5.0	-6.2	0.635
WAIS	-119.1±11.4	-113.7	0.997	-91.7±10.3	1.3	0.838
APIS	-0.4±7.2	-17.1	0.901	2.1±8.9	2.7	0.535

A similar comparison has been performed with the SMBA over the time period 1992-2017. With coefficients between 0.60 and 0.84, this correlation is lower, compared to GRACE, but still, the agreement is remarkable.

References

Arthern, R., Wingham, D., and Ridout, A.: Controls on ERS altimeter measurements over ice sheets: Footprint-scale topography, backscatter fluctuations, and the dependence of microwave penetration depth on satellite orientation, Journal of Geophysical Research – Atmospheres, 106, 33 471–33 484, https://doi.org/10.1029/2001JD000498, 2001.

Bamber, J., Gomez-Dans, J., and Griggs, J.: A new 1 km digital elevation model of the Antarctic derived from combined satellite radar and laser data – Part 1: Data and methods, The Cryosphere, 3, 101–111, https://doi.org/10.5194/tc-3-101-2009, 2009.

Brockley, D., Baker, S., Femenias, P., Martinez, B., Massmann, F.-H., Otten, M., Paul, F., Picard, B., Prandi, P., Roca, M., Rudenko, S., Scharroo, R., and Visser, P.: REAPER: Reprocessing 12 Years of ERS-1 and ERS-2 Altimeters and Microwave Radiometer Data, IEEE Trans. Geosci. Remote Sens., 55, 5506–5514, https://doi.org/10.1109/TGRS.2017.2709343, 2017.

Burton-Johnson, A., Black, M., Fretwell, P., and Kaluza-Gilbert, J.: An automated methodology for differentiating rock from snow, clouds and sea in Antarctica from Landsat 8 imagery: a new rock outcrop map and area estimation for the entire Antarctic continent, The Cryosphere, 10, 1665–1677, https://doi.org/10.5194/tc-10-1665-2016, 2016.

Davis, C., Kluever, C., and Haines, B.: Elevation Change of the Southern Greenland Ice Sheet, Science, 279, 2086–2088, https://doi.org/10.1126/science.279.5359.2086, 1998.

Fricker, H. and Padman, L.: Thirty years of elevation change on Antarctic Peninsula ice shelves from multimission satellite radar altimetry, J. Geophys. Res., 117, https://doi.org/10.1029/2011JC007126, 2012.

Fricker, H., Borsa, A., Minster, B., Carabajal, C., Quinn, K., and Bills, B.: Assessment of ICESat performance at the salar de Uyuni, Bolivia, Geophys. Res. Lett., 32, L21S06, https://doi.org/10.1029/2005GL023423, 2005.

Groh, A., Ewert, H., Rosenau, R., Fagiolini, E., Gruber, C., Floricioiu, D., Abdel Jaber, W., Linow, S., Flechtner, F., Eineder, M., Dierking, W., and Dietrich, R.: Mass, volume and velocity of the Antarctic Ice Sheet: present-day changes and error effects, Surv. Geophys., 35, 1481–1505, https://doi.org/10.1007/s10712-014-9286-y, 2014.

Helm, V., Humbert, A., and Miller, H.: Elevation and elevation change of Greenland and Antarctica derived from CryoSat-2, The Cryosphere, 8, 1539–1559, https://doi.org/10.5194/tc-8-1539-2014, 2014.

Ivins, E., James, T., Wahr, J., Schrama, E., Landerer, F., and Simon, K.: Antarctic contribution to sea level rise observed by GRACE with improved GIA correction, J. Geophys. Res. Solid Earth, 118, 3126–3141, https://doi.org/10.1002/jgrb.50208, 2013.

Legrésy, B., Rémy, F., and Schaeffer, P.: Different ERS altimeter measurements between ascending and descending tracks caused by wind induced features over ice sheets, Geophys. Res. Lett., 26, 2231–2234, https://doi.org/10.1029/1999GL900531, 1999.

Ligtenberg, S., Helsen, M., and van den Broeke, M.: An improved semi-empirical model for the densification of Antarctic firn, The Cryosphere, 5, 809–819, https://doi.org/10.5194/tc-5-809-2011, 2011.

McMillan, M., Shepherd, A., Sundal, A., Briggs, K., Muir, A., Ridout, A., Hogg, A., and Wingham, D.: Increased ice losses from Antarctica detected by CryoSat-2, Geophys. Res. Lett., 41, 3899–3905, https://doi.org/10.1002/2014GL060111, 2014.

Roemer, S., Legrésy, B., Horwath, M., and Dietrich, R.: Refined analysis of radar altimetry data applied to the region of the subglacial Lake Vostok / Antarctica, Remote Sens. Environ., 106, 269–284, https://doi.org/10.1016/j.rse.2006.02.026, 2007.

Scagliola, M., Fornari, M., Bouffard, J., and Parrinello, T.: The CryoSat interferometer: End-to-end calibration and achievable performance, Adv. Space Res., https://doi.org/10.1016/j.asr.2017.09.024, 2017.

Schröder, L., Richter, A., Fedorov, D., Eberlein, L., Brovkov, E., Popov, S., Knöfel, C., Horwath, M., Dietrich, R., Matveev, A., Scheinert, M., and Lukin, V.: Validation of satellite altimetry by kinematic GNSS in central East Antarctica, The Cryosphere, 11, 1111–1130, https://doi.org/10.5194/tc-11-1111-2017, 2017.

Siegfried, M., Hawley, R., and Burkhart, J.: High-Resolution Ground-Based GPS Measurements Show Intercampaign Bias in ICESat Elevation Data Near Summit, Greenland, Geoscience and Remote Sensing, IEEE Transactions on, 49, 3393–3400, https://doi.org/10.1109/TGRS.2011.2127483, 2011.

Whitehouse, P., Bentley, M., Milne, G., King, M., and Thomas, I.: A new glacial isostatic adjustment model for Antarctica: calibrated and tested using observations of relative sea-level change and present-day uplift rates, Geophys. J. Int., 190, 1464–1482, https://doi.org/10.1111/j.1365-246X.2012.05557.x, 2012.

Wingham, D., Rapley, C., and Griffiths, H.: New techniques in satellite altimeter tracking systems, in: ESA Proceedings of the 1986 International Geoscience and Remote Sensing Symposium(IGARSS'86) on Remote Sensing: Today's Solutions for Tomorrow's Information Needs,, vol. 3, pp. 1339–1344, Zürich, 1986.

Wingham, D., Ridout, A., Scharroo, R., Arthern, R., and Shum, C.: Antarctic Elevation Change from 1992 to 1996, Science, 282, 456–458, https://doi.org/10.1126/science.282.5388.456, 1998.